Nano Research

Open Access

Research Article

Bio-inspired flexible composite multilayer material: Cross-scale topological assembly for infrared-radar compatible detection suppression

Zhongru Ren[1], Hongcheng Yin[1] ✉, Changliang Zhang[2], Ming Fang[3], Lu Yan[3], Xin Sun[1], Junzhe He[1], and Xiaofang Liu[3] ✉

[1] *National Key Laboratory of Scattering and Radiation, Beijing 100854, China*
[2] *The First Representative Office Stationed in Beijing of KJDS, Beijing 100854, China*
[3] *School of Materials Science and Engineering, Beihang University, Beijing 100191, China*

Cite this article: *Nano Research*, **2025**, *18*, 94907833. https://doi.org/10.26599/NR.2025.94907833

ABSTRACT: The increasing demand for multi-spectral compatibility in complex electromagnetic environments has highlighted the critical challenge of reconciling infrared detection suppression with broadband microwave absorption. Inspired by the multilevel gradient structure of bamboo and the dynamic nanocrystal spacing modulation in chameleon skin, a flexible composite multilayer material is fabricated through a cross-scale topological assembly method. By constructing a functional coupling architecture comprising an infrared low-emissivity pattern layer, a broadband impedance matching layer, and a resistive frequency selective surface layer, effective energy suppression across both the infrared and radar spectra is achieved. The optimized structure demonstrates a reflection loss below −10 dB across a broad frequency range from 4.06 to 20.68 GHz, while maintaining an average infrared emissivity below 0.21 in the 8–14 μm wavelength range. Moreover, this structure exhibits high mechanical strength, a simple fabrication process, and stable performance, making it a promising candidate for next-generation multi-spectral detection applications.

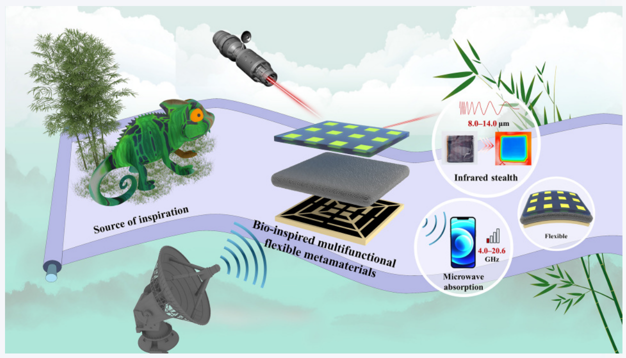

KEYWORDS: infrared-radar compatible detection suppression, broadband absorber, low-emissivity pattern, impedance matching layer

1 Introduction

With the rapid development of multi-spectral detection technology, traditional single-band absorbing materials are insufficient to meet the growing complexity of practical requirements [1]. Given the widespread application of infrared and radar detection technologies, there is an urgent need to develop compatible detection suppression structures. The essence of radar detection suppression lies in reducing the effective detection range of the radar [2], while infrared detection suppression is achieved by lowering the surface infrared emissivity or regulating thermodynamic heating process, thereby reducing the infrared radiation contrast between the target and the surrounding environment [3]. Due to the inherent differences in the physical mechanisms, it remains a huge challenge to achieve infrared-radar compatible detection suppression through a singular material [4]. Remarkably, this bottleneck has revealed sophisticated solutions through biological evolution. For instance, the moth-eye antireflective structure achieves broadband transmission regulation via subwavelength convex arrays. Inspired by this, Huang et al. designed a moth-eye-inspired multilayer material that realized compatibility for infrared-radar stealth [5]. Therefore, by analyzing the cross-scale collaborative regulation mechanisms in biological systems, the development of bio-inspired-hierarchical structure has become an effective approach to overcome the performance limitations of existing materials [6].

Traditionally, two main methods have been applied to fabricate infrared-radar compatible detection suppression materials. The first approach is to integrate radar absorbing materials with thermal-

Received: July 1, 2025; **Revised:** July 20, 2025
Accepted: July 22, 2025

✉Address correspondence to Hongcheng Yin, yinhc207@126.com; Xiaofang Liu, liuxf05@buaa.edu.cn

insulating materials [7]. For example, Wu et al. utilized a thermal reduction strategy to encapsulate copper sulfide with reduced graphene oxide, yielding a three-dimensional porous network composite aerogel [8]. The laminated porous architecture and multicomponent endowed aerogels with both thermal insulation and radar detection suppression. Experimental results demonstrated a minimum return loss of −55.1 dB with an effective absorption bandwidth of 7.2 GHz, while its infrared emissivity reached 0.6442. The second approach integrates photonic crystals with radar absorbers, where the bandgap of photonic crystals is adjusted to the infrared spectrum range to suppress infrared emission, while the radar absorbers ensure effective microwave energy absorption [9]. For instance, Zhang et al. fabricated a one-dimensional photonic crystal using Ge, ZnSe, and Si, and combined it with flexible radar-absorbing fabric to form a composite material [10]. This composite achieved a high reflectivity of 89.5% in the infrared wavelength range from 8 to 14 μm and a return loss of −24.5 dB at 14.6 GHz. However, these traditional materials generally suffer from limitations in radar absorption bandwidth and increased infrared emissivity [11]. Therefore, it is highly desirable to develop novel materials that integrate radar and infrared detection suppression functions [12].

The above approaches based on the material's intrinsic properties to achieve infrared-radar compatibility demands extensive time to optimize the filler's microstructure [13, 14]. However, composite materials can reduce design complexity at subwavelength scales while delivering superior electromagnetic performance [15]. Achieving infrared-radar compatible detection suppression with composite materials involves two primary physical mechanisms. The first approach combines a low-emissivity infrared coating with radar-absorbing composite materials [16]. For example, Zhang et al. proposed a radar-infrared compatible detection suppression composite material [17]. In the frequency range from 8.2 to 16.0 GHz, this structure achieves over 90% radar absorption, while maintaining an infrared emissivity as low as 0.2 in the 8–14 μm wavelength range. The second approach involves designing structures to control scattering energy, based on the concept of coding metamaterials [18]. For example, Meng et al. developed a random diffusion structure with low infrared emissivity and microwave scattering reduction [19]. The measured results indicate that the structure achieved a 10 dB backward scattering reduction from 3.8 to 6.8 GHz, while obtaining an infrared emissivity of 0.275. However, achieving infrared-radar compatible detection suppression through electromagnetic composite materials encounters notable obstacles. Firstly, inherent conflicts with in the physical mechanisms of radar-infrared compatible composite materials result in limitations such as narrow absorption bandwidth or undesirably high infrared emissivity [20]. Secondly, most composite material designs overlook the mechanical properties, thereby hindering their viability in practical engineering applications [21, 22].

Inspired by the gradient structural characteristics of bamboo, we propose a three-layer composite material, consisting of an infrared low-emissivity pattern layer at the top, a broadband impedance matching layer in the middle, and a resistive frequency selective surface (RFSS) at the bottom. This bio-inspired design effectively reduces interfacial reflections at heterogeneous material junctions through a gradient impedance matching mechanism, thereby extending the microwave absorbing bandwidth. Based on the biological mechanisms of chameleons, which dynamically modulate light propagation via reorganization of dermal photonic crystal nanostructures, we achieve dual-spectral wavefront manipulation by optimizing the sub-wavelength geometric parameters of infrared low-emissivity patterns. The composite structure maintains an average emissivity of 0.206 in the 8–14 μm wavelength range and achieves a return loss of −10 dB within the operational bandwidth from 4.06 to 20.68 GHz (corresponding to a 134.4% fractional bandwidth). Furthermore, compression tests reveal an impressive elastic modulus as high as 12.6 MPa, demonstrating excellent mechanical properties that substantially improve the stability and durability of the structure under operational conditions.

2 Experimental section

2.1 Materials

Diphenylmethane diisocyanate (MDI), epoxy resin, polyether polyol (M_W = 3000), triethylbenzylammonium chloride catalyst, methyl silicone oil demolding agent, polyurethane (PU) foaming agent, and carbon black (CB) powder were purchased from Hunan Aoke New Material Technology Co., Ltd. Flaky aluminum powder, water-based PU resin, phenolic resin, polyimide (PI) film, polyethylene terephthalate (PET) film, polypropylene (PP) foam, the specialized curing agent (YC-2820), and the film-forming additive (Novares LA-300W) were purchased from Shenzhen Jiadida New Material Technology Co., Ltd. All chemicals were used without further purification.

2.2 Preparation of the infrared low-emissivity pattern

Flaky aluminum powder was added to the water-based PU resin and then ultrasonically dispersed for 10 min. The curing agent and the film-forming additive were added to the above system to adjust the viscosity. Subsequently, the whole system was ultrasonically dispersed for another 15 min before being poured into the hopper of a spray gun. The spraying pressure was set to 0.5 MPa, and the speed was maintained at 4 cm/s, ensuring that the wet coating was evenly attached to the PI film. After drying at 85 °C for 12 h, an infrared low-emissivity coating was prepared. Finally, the periodic patterns with specific geometric dimensions were fabricated by laser etching technique, achieving a precision of 0.01 mm.

2.3 Preparation of the broadband impedance matching layer

The broadband impedance matching layer positioned at the middle of the proposed multilayer structure exhibits dual functionality: enhancing compressive mechanical rigidity and optimizing gradient impedance performance. Its fabrication process comprises three sequential stages: (i) synthesis of epoxy-isocyanate prepolymer. The reaction follows a two-step procedure. In the first step, MDI and polyether polyol were reacted at a controlled NCO/OH molar ratio of 2.5 and a temperature of 80 °C for 1 h to yield an NCO-terminated prepolymer. Upon reaction completion, epoxy resin and triethylbenzylammonium chloride catalyst were added. The resulting mixture reacted at 80 °C for 2 h, during which the epoxy groups reacted with the residual isocyanate groups, yielding mixture II. The reaction significantly increased the crosslink density of the polymer network. (ii) Homogeneous dispersion of CB powder. As the absorbent, CB particles are prone to agglomeration due to van der Waals force. To improve their dispersibility, a chemical modification process was implemented. The CB powder underwent reflux oxidation for 4 h at 80 °C in 65 wt.% nitric acid solution. Subsequently, the treated CB were esterified with polyether polyol for 2 h at 120 °C. Finally, the modified particles were dispersed uniformly using a high-shear homogenizer operating at 3000 rpm for 15 min, yielding the mixture II. (iii) Foaming and post-processing. Mixture I, mixture II, and the PU foaming agent were ultrasonically dispersed for 10 min to prepare homogeneous foaming slurry. A preheated aluminum mold (coated with methyl silicone oil release agent) served as the reaction vessel. The prepared slurry was then poured into the mold and foamed at 80 °C for 1.5 h. After demolding, the sample was precision-trimmed to final dimensions of 300 mm × 300 mm × 4 mm, producing a standardized rectangular block.

2.4 Preparation of the resistive frequency selective surface

The PET film was used as the substrate. Surface impurities were removed using acetone, and adhesion was enhanced by sanding the substrate. The indium tin oxide (ITO) target was mounted inside the magnetron sputtering apparatus. Under vacuum conditions, high-purity argon gas was introduced, allowing ITO ions to form a thin film of specified thickness on the substrate. After drying at 85 °C for 6 h, the resistive ITO film was obtained. The periodic pattern coordinate data were input into the laser etching system, enabling the fabrication of a RFSS with dimensions of 300 mm × 300 mm. Following the etching process, the manufactured RFSS was subsequently bonded to a polypropylene (PP) foam substrate using adhesive lamination.

2.5 Characterizations

The phase compositions of the samples were obtained by an Olympus X-5000 X-ray diffractometer (XRD) using Cu target as the irradiation source. The infrared emissivity curve of the sample within the 8–14 μm wavelength range was measured using a Bruker v70 infrared spectrometer. The microstructure was characterized by a Quanta FEG field scanning electron microscopy (SEM). To measure the electromagnetic parameters of the samples, the absorbents were mixed with molten paraffin wax in proportion using a mold to obtain a coaxial test specimen (the outer diameter is 7 mm, and the inner diameter is 3.04 mm). Then, the coaxial specimen was plugged into the measurement system using a special fixture and connected to the two ports of the vector network analyzer (Rohde & Schwarz-ZVA40) through two low-loss cables. The monostatic radar cross section (RCS) characteristics of the sample were evaluated in an anechoic chamber through the following procedure: (1) The vector network analyzer required preheating prior to use. (2) Transmit and receive antennas were positioned at a far-field distance from the target with mutual azimuthal offset < 5°. (3) Scattering parameters were measured for both the empty chamber and a calibration corner reflector. (4) The sample was mounted on one reflective surface of the corner reflector. Besides, the broadband monostatic RCS reduction value was calculated as the difference between the calibration corner reflector and the sample. The experimental configuration for determining return loss closely parallels the standard RCS measurement setup. Specifically, return loss is quantified as the logarithmic value of the ratio between the reflected power magnitudes from the sample and a PEC plate.

3 Results and discussion

Bamboo exhibits a multilevel composite architecture at the macroscopic scale, serving as a typical natural example of structural optimization. As illustrated in Fig. 1, the bamboo culm demonstrates a biologically gradient distribution across its nodal segments. Tapered tubular periodic nodes, positioned between adjacent segments, effectively stabilize the macroscopic morphology through geometrically optimized mechanisms [23]. Taking advantage of the gradient structural distribution observed in bamboo, we proposed a bio-inspired composite multilayer material consists of three functional layers: an upper infrared low-emissivity layer, a middle broadband impedance matching layer, and a lower resistive selective surface (FSS).

Figure 1 describes the brief preparation process of composite

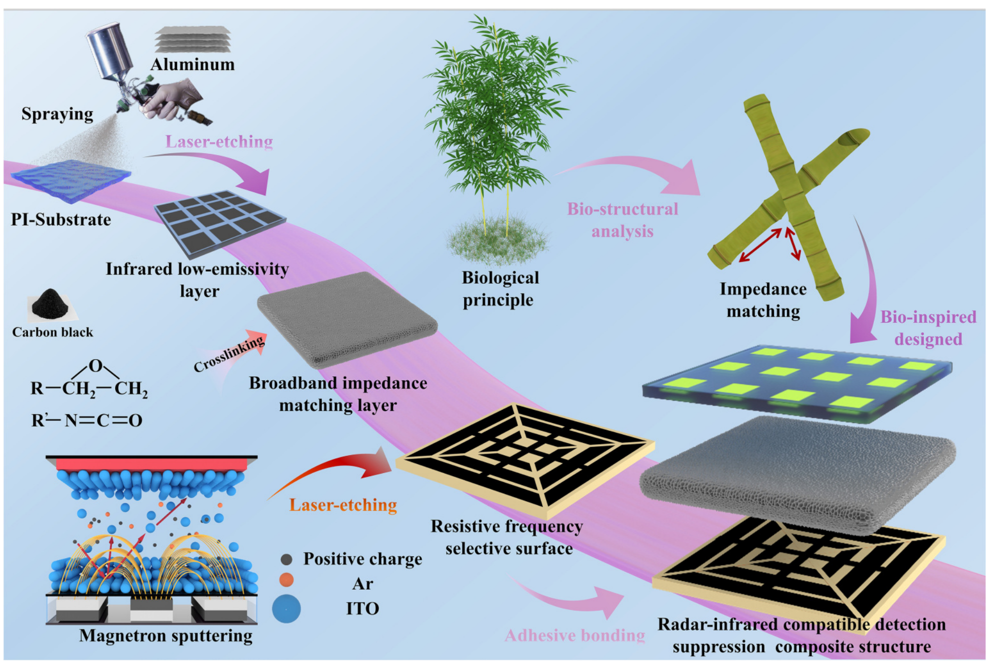

Figure 1 Schematic illustration of the bio-inspired composite multilayer material and the brief fabrication processes of each constituent layer.

multilayer structure, the infrared low-emissivity coating was fabricated using a combination of spray coating and laser etching. A mixture of flaky aluminum, water-based PU resin, curing agent and film-forming additives (with controlled viscosity) was spray-coated onto a PI substrate and then cured. Laser etching was subsequently applied to the surface of the coating to create square periodic patterns, which enhanced its infrared low-emissivity properties while ensuring microwave transmission through the layer [24]. To improve the broadband impedance matching between composite structures and free space, the middle layer is composed of modified PU foam filled with CB particles. The mechanical properties of the modified PU foam were enhanced through cross-linking reactions [25, 26], providing excellent elasticity. The RFSS layer enables flexible manipulation of absorption mechanisms through diverse geometric configurations, achieving efficient electromagnetic energy dissipation functions [27]. ITO-PET films with specific sheet resistance were first deposited via magnetron sputtering [28], followed by the fabrication of precise periodic patterns through laser etching techniques. Finally, the three-layer composite material was integrated through adhesive bonding, with a total thickness of 7.8 mm.

For the infrared low-emissivity pattern layer situated at the top of the composite structure, Fig. 2(a) illustrates its biomimetic design methodology. In the skin of chameleons, guanine crystals are arranged in a face-centered cubic lattice. When stimulated by external environment, these crystals change their color by increasing the spacing between the nanocrystals, thereby achieving camouflage [29]. Inspired by this approach, we first cured the slurry of the "flaky aluminum and water-based PU resin" system into a coating, then utilized laser etching technique to prepare square-pattern periodic arrays with specific geometric parameters, simultaneously achieving the dual macroscopic properties of infrared low-emissivity and radar high-transmittance. The functionality of infrared low-emissivity coatings is attained by modifying both the ball-milling duration of flaky aluminum powder and the mass fraction of these fillers (as shown in Table S1 in the Electronic Supplementary Material (ESM)). Figures 2(b)–2(e) present SEM images of the samples (SEM images with higher magnification are shown in Fig. S1 in the ESM). Examination of varied SEM micrographs demonstrates that extended ball milling duration leads to a marked increase in the average diameter of flaky aluminum particles. This enlargement, coupled with a higher proportion of larger flakes by mass, promotes microstructural compaction. This densification, attributable to both factors, substantially increases the reflection efficiency of incident infrared radiation towards free space, resulting in suppressed infrared emissivity. Figure 2(f) can also verify this microscopic phenomenon. In the wavelength range of 8–14 μm, Al-16h-25 wt.%

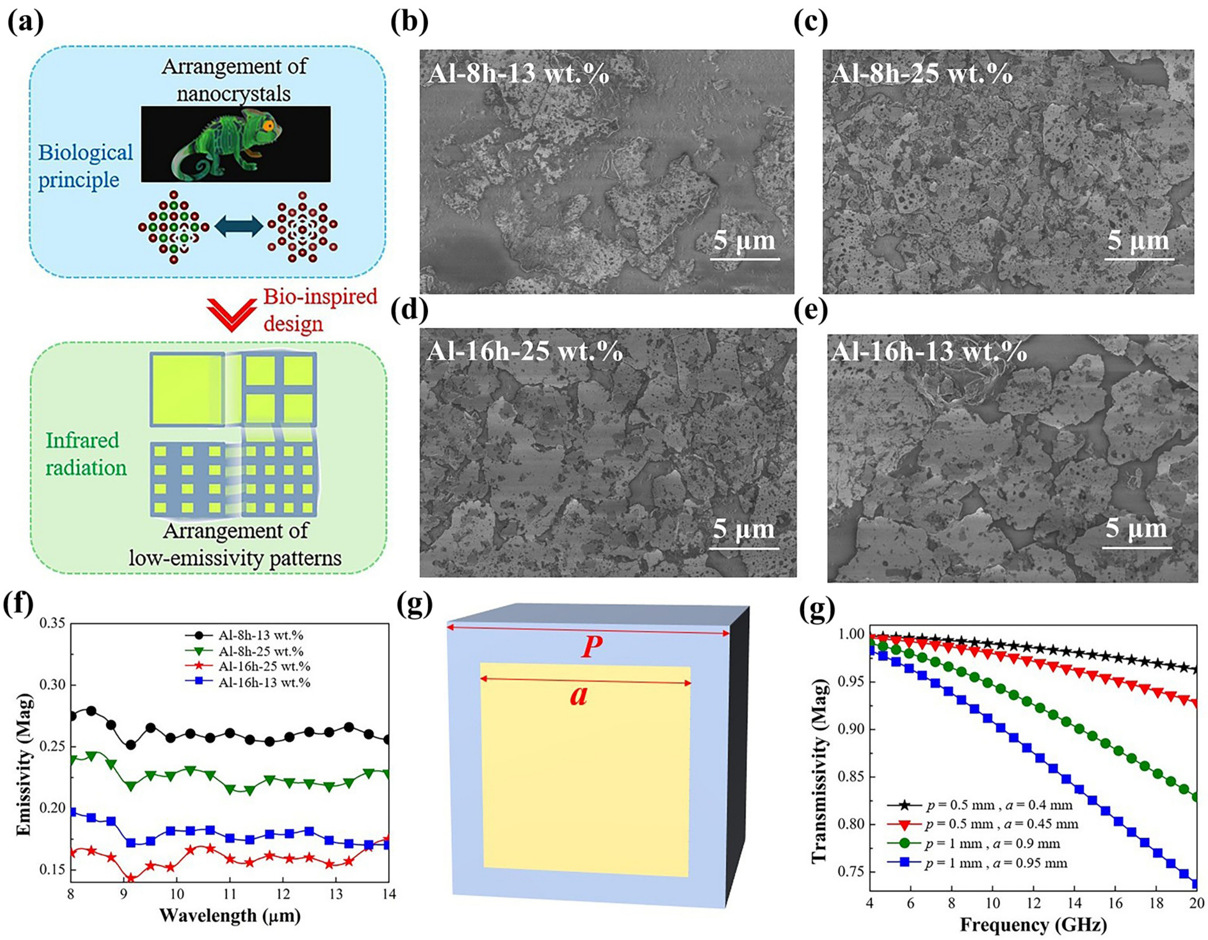

Figure 2 (a) The correlation between the arrangement of nanocrystals in chameleon skin and the design process of infrared low-emissivity periodic patterns. (b)–(e) SEM images of the coating samples. (f) Measurements of the infrared emissivity of coating samples within the 8–14 μm wavelength range. (g) Structural schematic of the basic unit in the infrared low-emissivity layer. (h) The correspondence relationship between geometric parameters of basic units in the infrared low-emissivity layer and radar wave transmissivity.

with the densest microstructure exhibits the lowest infrared emissivity, ranging from 0.14 to 0.17 (measurement setup for the infrared emissivity is shown in Fig. S2 in the ESM). Furthermore, Fig. S3 in the ESM confirms that the ball milling process flattens the aluminum powder into a flaky morphology without altering its phase structure. Based on these results, we selected Al-16h-25 wt.% as the optimal infrared low-emissivity coating.

To achieve the combined functionalities of low infrared emissivity and high radar wave transparency, the top-layer coating was etched into a periodic square-patterned array. On the one hand, the density of these square patterns plays a crucial role in radar wave transmission. An excessively dense arrangement can lead to impedance mismatch between the top layer and free space, thereby reducing radar transmissivity. As shown in Figs. 2(g) and 2(h), when the unit period p = 0.5 mm, and the geometric parameter a = 0.4 mm/0.45 mm, the radar transmissivity exceeds 94% within the operational bandwidth. On the other hand, the infrared emissivity of the composite structure is significantly influenced by the material properties of the top layer. According to the Kirchhoff's law, the total infrared emissivity can be expressed as

$$\varepsilon_{\text{total}} = \varepsilon_{\text{Al}} \times t + \varepsilon_{\text{PI}} \times (1-t) \tag{1}$$

where $\varepsilon_{\text{total}}$, ε_{Al}, ε_{PI} and t denote the infrared emissivity of the composite structure, the flaky aluminum coating, the PI substrate, and the coverage ratio of flaky aluminum coating, respectively. As for the proposed composite structure, the global infrared emissivity was predominantly manipulated by the coverage ratio of the low-emissivity patterns [30]. Numerical simulations demonstrated that when geometric parameters were optimized at p = 0.5 mm and a = 0.45 mm, the calculated infrared emissivity of the composite structure reached 0.216.

The proposed broadband impedance matching layer plays a crucial role in achieving compatibility between infrared and radar frequency bands. Moreover, due to its highly porous structure, the foam exhibits apparent density of only 9 mg/cm^3, allowing it to rest on leaves (Fig. 3(a)). The compression-recovery behavior of the foam was tested using an electromechanical universal testing machine (as presented in Fig. 3(b)). When the sample was compressed to 40% strain, it could rapidly recover to is original height within 2.67 s upon pressure release, demonstrating its good elasticity. To assess its mechanical strength, the foam was subjected to a load of 100 grams. It retained its original shape throughout the 5 min test duration (Fig. 3(c)). By adjusting the equivalent permittivity and thickness of the broadband matching layer, the input impedance of the composite structure can be optimized [31]. The Maxwell-Garnett model is suitable for describing the effective permittivity of microporous foam structures [32]

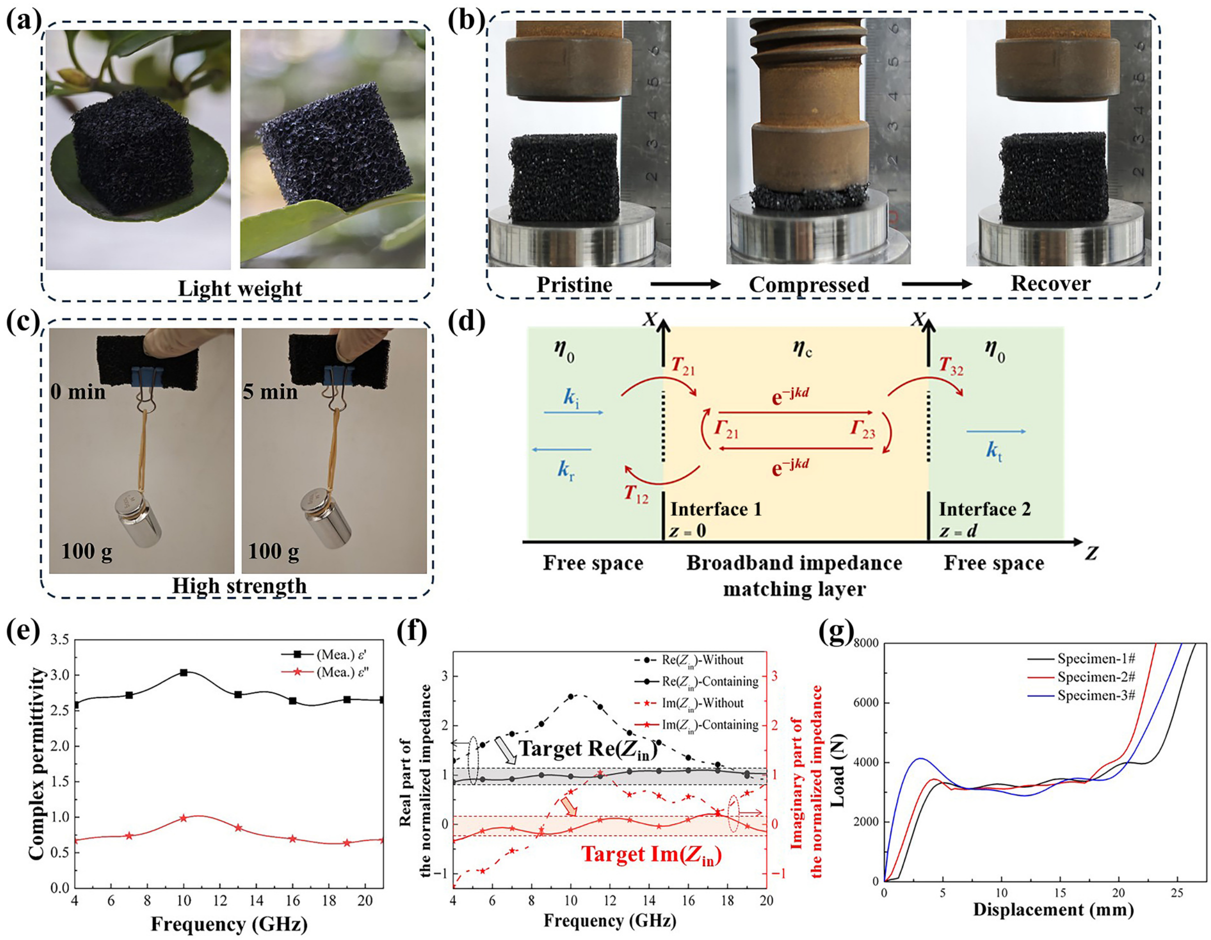

Figure 3 Physical characteristics of the proposed broadband impedance matching layer. (a) Light weight, (b) compressibility and recovery, (c) tensile strength, (d) schematic illustration of the reflection-transmission model, (e) measured complex permittivity of proposed broadband impedance matching layer, (f) comparison of real and imaginary parts of normalized impedance for proposed structure, containing vs. without broadband impedance matching layer, and (g) displacement-load curves of the prepared specimens.

$$\varepsilon_{\text{eff}}^{\text{MG}} = \left[\frac{(\varepsilon_2 + 2\varepsilon_1) + 2p(\varepsilon_2 - \varepsilon_1)}{(\varepsilon_2 + 2\varepsilon_1) - p(\varepsilon_2 - \varepsilon_1)} \right] \varepsilon_1 \tag{2}$$

where ε_1, ε_2, and p are the permittivity of the solid phase and air phase, and the volume fraction of air phase in the porous structure, respectively. Therefore, the addition of CB powder during the foaming process facilitates the adjustment of the permittivity of the broadband impedance matching layer, which enhances penetration of electromagnetic waves into the composite structure. Following the interface impedance analysis of heterogeneous structures outlined in Fig. 3(d), the reflection-transmission model provides a framework for analyzing the propagation behavior of electromagnetic waves within the broadband impedance layer. The reflection and transmission coefficients are defined as follows [33]

$$\gamma(z=0) = \frac{\Gamma_{12} + \Gamma_{23}\text{e}^{-\text{j}2kd}}{1 + \Gamma_{12}\Gamma_{23}\text{e}^{-\text{j}2kd}} \tag{3}$$

$$\tau(z=d) = \frac{(1+\Gamma_{12}) + (1+\Gamma_{23})\text{e}^{-\text{j}2kd}}{1 + \Gamma_{12}\Gamma_{23}\text{e}^{-\text{j}2kd}} \tag{4}$$

where τ and γ denote the reflection and transmission coefficients, respectively. Adjusting the permittivity of the broadband impedance matching layer is crucial for controlling the propagation wave vector $\boldsymbol{k}$ within the structure [34]. Additionally, the optimal thickness d can be derived using the $\lambda/4$ cancellation theory [35, 36]

$$d = \frac{(2m+1)c}{nf}\left(\frac{1}{4} + \Delta\right) \quad (m = 1, 2, 3, \ldots) \tag{5}$$

where f is the resonant frequency, m is the natural integer, and n is the refractive index, and Δ can be expressed as

$$\Delta = \frac{h\sinh(t\pi)}{4\pi(1 - ht\cosh(t\pi))} \tag{6}$$

where $t = a/n$, and a is extinction coefficient, $h = [t - \tan(\delta_{\text{m}})]/[1 + t\tan(\delta_{\text{m}})]$, $\tan(\delta_{\text{m}})$ is the magnetic loss tangent.

As shown in Fig. S4 in the ESM, at a center frequency of f_0 = 12 GHz, the optimal impedance matching performance is achieved with a thickness of d = 3.3 mm. Following the measurement results in Fig. 3(e), the permittivity of the broadband impedance matching layer was measured using the free-space method when the mass fraction of CB powder reached 15 wt.% (the required measuring equipment is shown in Fig. S5 in the ESM). Besides, the complex permeability of the broadband impedance matching layer was also measured, as demonstrated in Fig. S6 in the ESM, the results confirm the absence of magnetic loss mechanism in this layer. To further elucidate the role of the proposed structure in the regulation of broadband impedance, the relationship between the scattering matrix and the transmission matrix of a two-port network was established from a macroscopic perspective using the S-parameter inversion method [37]. This approach enabled the derivation of the normalized impedance, which is expressed as follows:

$$Z_{\text{eff}} = \sqrt{\frac{(1+S_{11})^2 - S_{21}^2}{(1-S_{11})^2 - S_{21}^2}} \tag{7}$$

The scattering parameters of the proposed multilayer material were simulated using CST Microwave Studio. Impedance values were compared for the two configurations with and without the broadband impedance matching layer. Using Eq. (7), the normalized impedance values were calculated (Fig. 3(f)). For the structure with the matching layer, the real part of the equivalent impedance from 4 to 20 GHz approaches 1.0, while the imaginary part reaches 0. This demonstrates excellent impedance matching with free space across the operating bandwidth, facilitating efficient absorption of incident radar waves [38]. This compatibility enhances the entry of microwaves into the absorber, thereby improving absorption efficiency. During the foaming process, epoxy resin was utilized to modify the PU foam, forming a polyurethane-epoxy interpenetrating polymer network [39]. This structural modification significantly enhanced the mechanical properties of the broadband impedance matching layer. Figure 3(g) presents the load-displacement curves of three modified PU foam specimens. The curves demonstrate that the modified PU foam undergoes three distinct stages during uniaxial compression: elastic deformation, plastic collapse and densification. The elastic moduli of three cubic specimens (60 mm × 60 mm × 30 mm) were calculated as 12.3, 12.4, and 13.1 MPa. Accordingly, the average elastic modulus of the modified PU foam was determined to be 12.6 MPa.

The primary function of the resistive FSS structure is to maximize the dissipation of microwave energy across its operational bandwidth [40]. As a sub-wavelength structure, the period length (t) of the FSS typically satisfies $t \in [\lambda_{\text{L}}/7, \lambda_{\text{L}}/5]$, where λ_{L} denotes the lower cutoff wavelength, while its thickness (h) satisfies $h \in [\lambda_{\text{L}}/6, \lambda_{\text{L}}/4]$ [41]. For the lower cutoff frequency of 4 GHz (corresponding wavelength λ_{L}= 75 mm), the geometrical parameters are set as h= 3 mm, t = 15 mm, as illustrated in Fig. 4(a). The remaining geometric parameters govern the microwave absorption characteristics across different operational frequency bands. The optimal parameter configuration, determined through comprehensive parameter scanning, is defined as: L_1= 14.2 mm, W_1 = 1.9 mm, L_2 = 9.8 mm, W_2 = 1.7 mm, L_3 = 7.8 mm, W_3 = 0.8 mm, and β = 45°. The equivalent circuit method (ECM) is a widely used to quantify the input impedance of multilayer materials. When induced currents pass through conductive branches, they can be modeled as an effective inductance L_{eff}. Due to charge accumulation, a potential difference arises between adjacent conductive branches, which can be equivalently modeled as a capacitor C_{eff}. The ITO film, with its conductive losses, facilitates the dissipation of microwave energy and can be modeled as a resistor R_{eff}. Since the equivalent circuit parameters of resistive FSS structures are correlated with geometric parameters and loss characteristics, the actual values of C_{eff} = 0.574 pF, L_{eff} = 72.64 pH, and R_{eff} = 147.2 Ω can be accurately extracted using ADS software through parameter fitting techniques. According to transmission line theory, the effective input impedance Z_{in} of the resistive FSS can be expressed as:

$$Z_{\text{in}} = \frac{Z_{\text{FSS}} \cdot Z_{\text{h}}}{Z_{\text{FSS}} + Z_{\text{h}}} = \frac{Z_{\text{FSS}} \cdot \text{j}Z_0\sqrt{\frac{\mu_{\text{r}}}{\varepsilon_{\text{r}}}}\tan(k_0\sqrt{\mu_{\text{r}}\varepsilon_{\text{r}}}h)}{Z_{\text{FSS}} + \text{j}Z_0\sqrt{\frac{\mu_{\text{r}}}{\varepsilon_{\text{r}}}}\tan(k_0\sqrt{\mu_{\text{r}}\varepsilon_{\text{r}}}h)} \tag{8}$$

$$Z_{\text{FSS}} = \frac{R_{\text{sq}}S_1}{S_2} + \text{j}\omega L_{\text{eff}} + \frac{1}{\text{j}\omega C_{\text{eff}}} \tag{9}$$

where Z_{FSS} denotes the characteristic impedance of the resistive pattern, while Z_{h} represents the characteristic impedance of the dielectric layer. Z_0 is the characteristic impedance of free space, and R_{sq} is the square resistance of the ITO film. S_1 refers to the surface

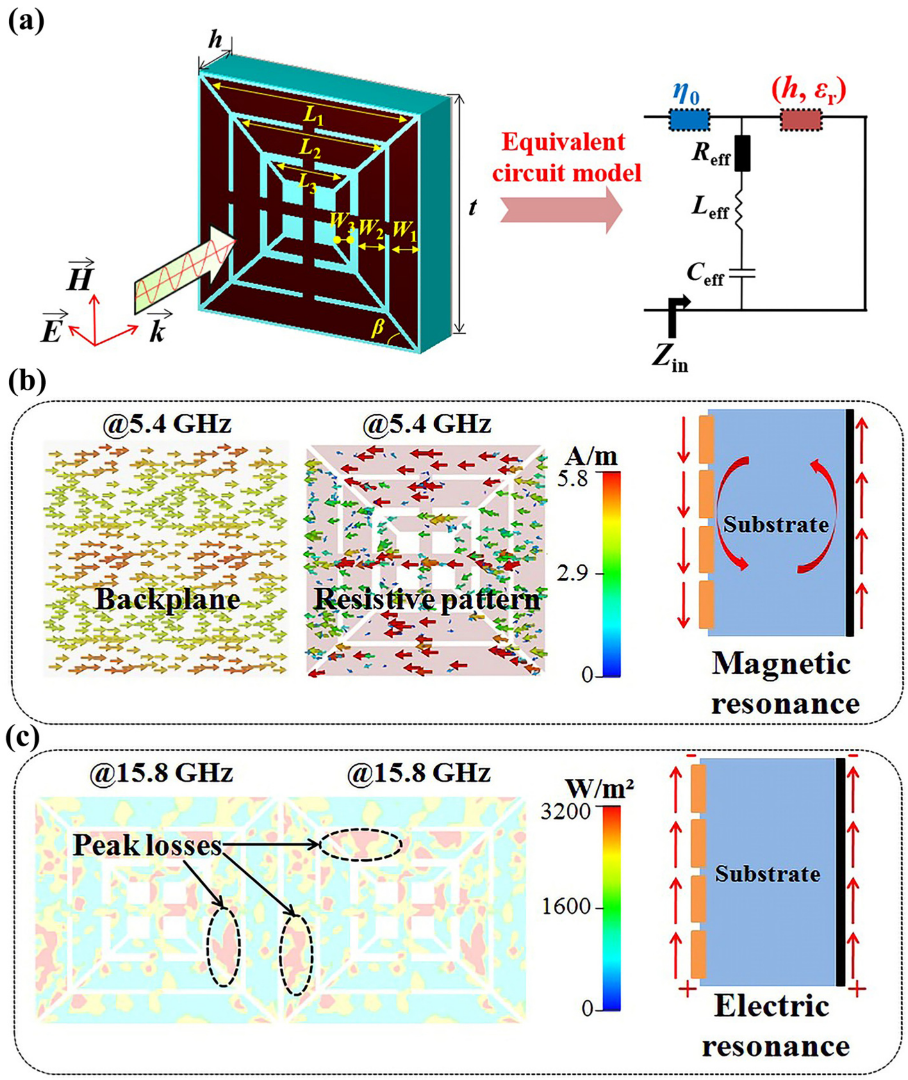

Figure 4 (a) Correspondence between the resistive FSS and the equivalent circuit model; (b) Surface current distribution and magnetic resonance of the resistive FSS at 5.4 GHz; (c) Surface energy loss and electric resonance of the resistive FSS at 15.8 GHz; (c) Correspondence between the resistive FSS and the equivalent circuit model.

area of the top layer, and S_2 is the actual area through which the surface current flows. The angular frequency of the incident microwaves is denoted by ω, h is the thickness of the substrate layer, ε_r and μ_r are the relative permittivity and permeability of the substrate layer, respectively. To achieve perfect absorption of microwave energy, it is essential that Z_{in} equals Z_0. Therefore, the impedance matching parameters should satisfy the following conditions [42]

$$R_{sq} = \frac{2Z_0 L^2 \sin^2(k_0 h)}{p^2} \quad (10)$$

$$b_1 = \frac{1}{\omega C_{eff}} - \omega L_{eff} = \frac{Z_0 \sin(2k_0 h)}{2} = b_2 \quad (11)$$

Equations (10) and (11) outline the matching conditions for the real and imaginary parts of the input impedance, respectively. As shown in Fig. S7 in the ESM, the intersection of b_1 and b_2 at frequencies f_1 = 5.4 GHz and f_2 = 15.8 GHz indicates that the imaginary parts of the input impedance are matched at these frequencies, suggesting the presence of two potential absorption peaks. Calculations reveal that when the sheet resistance of the ITO film is set to R_{sq} = 75 Ω/sq, the real part of the impedance at the absorption peak frequency can be matched.

To better understand the electromagnetic loss mechanisms in resistive FSS, we analyzed the distribution of surface currents and energy dissipation. Following the simulation results outlined in Fig. 4(b), at the first resonance frequency of f_1 = 5.4 GHz, the surface currents are uniformly distributed across the branches of the resistive pattern. The current direction in the resistive pattern is opposite to that in the backplane, inducing magnetic resonance. Consequently, microwave energy is dissipated within the substrate. As illustrated in Fig. 4(c), at the second resonance frequency of f_2 = 15.8 GHz, most of the surface energy dissipation is concentrated at the edges of each branch in the patterned layer. The adjacent branches behave like parallel-plate capacitors, and the currents in the resistive pattern and the backplane flow in the same direction, thereby inducing electrical resonance.

To evaluate the microwave absorption performance of the proposed composite structure, adhesive films were used to bond the three functional layers into a composite structure with dimensions of 300 mm × 300 mm × 7.8 mm. As shown in Fig. 5(a), due to the

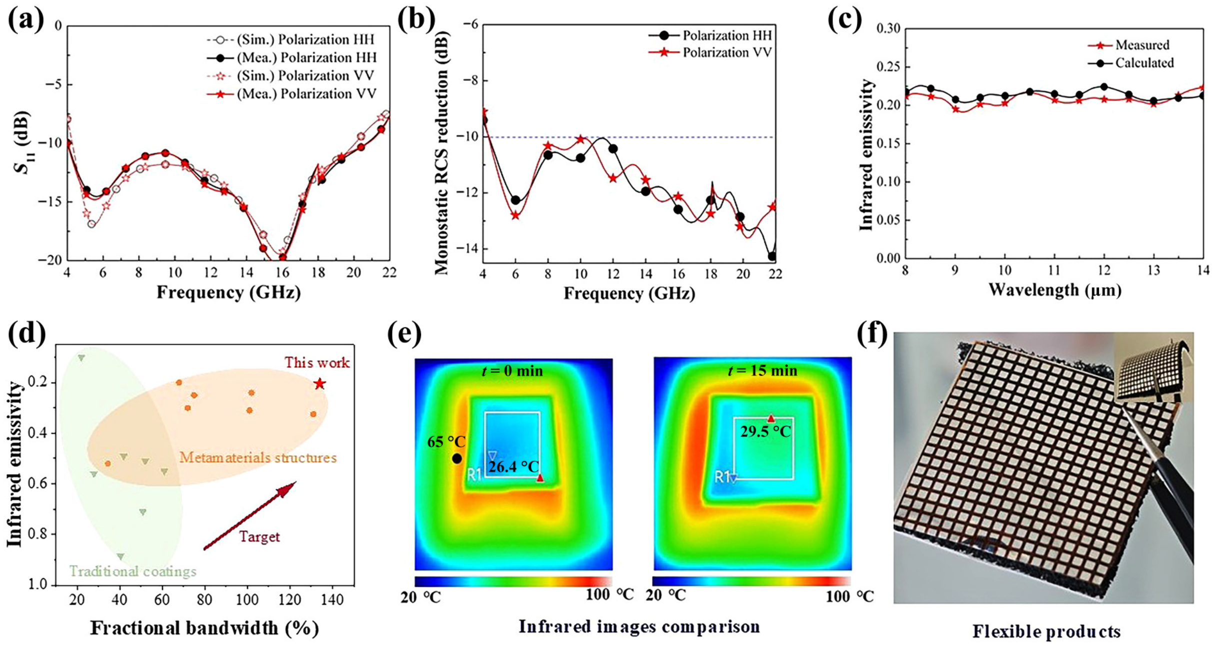

Figure 5 (a) Comparison of simulated and measured return loss S_{11} for the proposed structure under different polarization conditions. (b) Measured monostatic RCS reduction performance of the proposed structure under HH and VV polarization conditions. (c) Comparison of measured and calculated infrared emissivity for proposed multilayer material across the 8–14 μm wavelength range. (d) Comparison of fractional bandwidth and infrared emissivity between this work and previously reported structure. (e) IR images of proposed composite metasurface heated at 65 °C over time. (f) Preparation of the product and demonstration of its flexibility.

centrosymmetric characteristics of all unit cell patterns within the structure, the simulated S_{11} parameters are identical for both co-polarized (horizontal-horizontal (HH) and vertical-vertical (VV)) incident waves, demonstrating exceptional polarization insensitivity. The minor differences between the measured results for HH and VV polarization modes originate from the non-ideal isotropic characteristics of the broadband impedance matching layer. The measured S_{11} remains below −10 dB from 4.06 to 20.68 GHz, corresponding to a relative bandwidth of 134.4%. A comparative analysis of bistatic RCS images at 15 GHz indicates that the proposed structure consistently achieves RCS reduction across a pitch range from −72° to 72° (Fig. S9 in the ESM). The experimental results presented in Fig. 5(b) demonstrate that the proposed composite material achieves a monostatic RCS reduction exceeding 10 dB from 4.42 to 20 GHz (measurement principle is shown in Fig. S8 in the ESM). This performance remains consistent under both HH and VV polarization conditions. However, the discrepancies between the measured and simulated microwave absorption performance of the sample can be attributed to three primary factors. First, the sample was bonded using an adhesive film, its impact on the radar absorption performance was not considered in the simulations. Second, the ITO film in the resistive FSS structure was fabricated using magnetron sputtering, where the non-uniform sputtering thickness may lead to errors in the average sheet resistance. Third, the simulations were conducted under idealized boundary conditions, whereas the actual sample had finite dimensions, leading to edge effects during measurements.

To verify the infrared capabilities of the composite structure within the 8–14 μm wavelength range, a 40 mm × 40 mm fragment was cut from the sample and placed in the infrared spectrometer. As shown in Fig. 5(c), the measured infrared-emissivity of the sample fluctuated between 0.192 and 0.227, with an average emissivity of 0.206. A close correspondence is evident between the measured and calculated infrared-emissivity of the fabricated sample. Notably, as illustrated in Fig. 5(d), compared to previously reported metamaterial structures [43–48] and traditional coatings [49–54], the proposed composite structure exhibits the combined advantages of a broad operational bandwidth and low infrared emissivity. As shown in Fig. 5(e), the proposed composite material demonstrates reliable infrared stealth performance. After being heated on a 65 °C heat source for 15 min, the maximum temperature of the sample only increased by 3.1 °C. The physical photograph of the composite material is presented in Fig. 5(f), as each constituent layer consists of flexible materials, the integrated structure exhibits exceptional bending compliance. This distinctive mechanical adaptability demonstrates significant potential for application in conformal integration with irregularly shaped surfaces. Moreover, to evaluate the functional stability of the proposed structure under diverse environmental conditions, we performed thermal shock, scratch resistance, and salt spray tests on the samples. First, the thermal shock resistance was evaluated using a nitrogen-purged thermal shock test chamber (TSG-71S-W). The specimen was placed on the central partition and subjected to 20 thermal shock cycles between temperatures of −55 and 85 °C (4 min per cycle). Macroscopic examination revealed no observable surface deterioration. Subsequently, a 0.5 mm-diameter cemented carbide indenter was used to apply a normal load of 5 N. At a constant scratching speed of 3 mm/s, the resulting linear scratch depth on the surface layer was measured via laser profilometry, yielding a value of only 3.6 μm. Finally, the corrosion resistance was evaluated using a C&W salt spray chamber. The specimen was continuously exposed to a 5 wt.% NaCl solution spray at a constant temperature of 35 °C for 100 h, and no significant blistering or corrosion was observed. These experimental results confirm the expected service life of the novel multilayer structure.

Based on the preceding experiments and simulations, the physical mechanisms enabling the composite structure to achieve infrared-radar compatible detection suppression are revealed from multiple perspectives [55–58], as illustrated in Fig. 6.

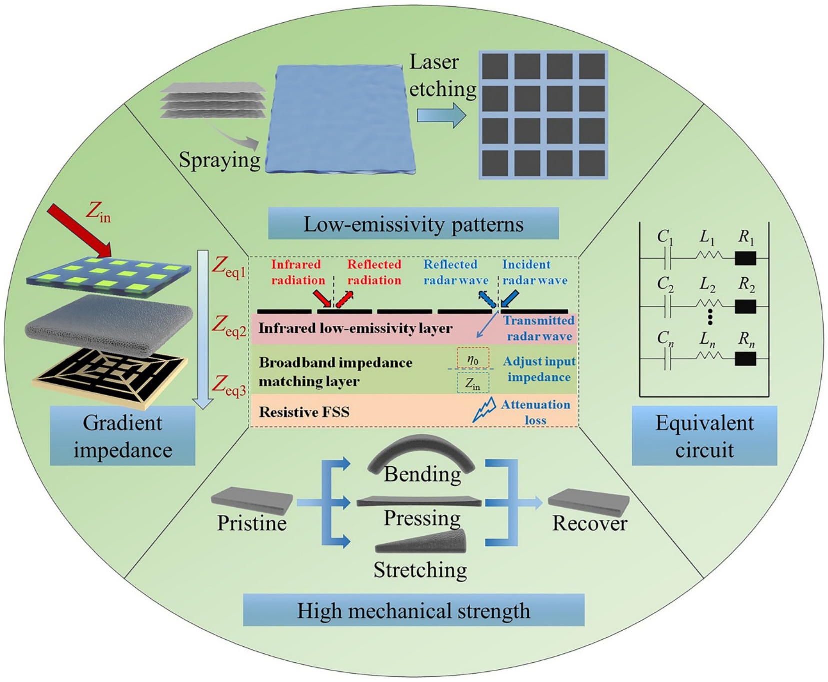

Figure 6 Schematic diagram of the proposed composite structure that simultaneously achieves infrared low-emissivity and broadband microwave absorption.

(i) The top layer of the composite structure serves two key functions. First, it reflects a higher proportion of infrared waves, achieved by optimizing the compatibility between flaky aluminum particles and water-based PU resin. The aluminum flakes, suspended on the surface of the water-based PU resin, form a dense film effectively reduces infrared emissivity. Second, laser-etched gaps in the top layer enable microwaves to propagate through and enter the composite structure, facilitating energy dissipation.

(ii) The key challenge in achieving broadband microwave absorption lies in the significant disparity between the geometric dimensions of the top layer's low emissivity patterns and the bottom layer's resistive FSS, resulting in impedance mismatch. To address this, a broadband impedance matching layer was introduced, incorporating a specific proportion of carbon black (CB) during the foaming process [59–61]. This addition induces a gradient impedance effect throughout the structure, thereby enhancing the broadband impedance matching. Moreover, the three-dimensional network formed by CB-modified PU system significantly improves the mechanical properties of the proposed composite structure, ensuring both durability and structural integrity.

(iii) The main function of the resistive FSS is to absorb microwave energy. In composite multilayer material design, equivalent inductance and capacitance are introduced by optimizing geometric parameters. Equivalent resistance is achieved through the conductive losses of the ITO film, forming multiple parallel equivalent RLC circuits [62–65]. By simply adjusting the geometric parameters, variations in operational bandwidth and absorption amplitude can be achieved, thereby enhancing design flexibility.

4 Conclusion

Inspired by the gradient structure of bamboos and the nanocrystal distribution in chameleons' dermis, this work proposes a composite multilayer structure that achieves the integration of infrared low-emissivity and broadband radar absorption performances. The composite material achieves an average emissivity of 0.206 within the 8–14 μm infrared wavelength range, enabled by laser-etched square patterns on the top layer. Moreover, the microwave absorption mechanism is achieved through gradient impedance matching to suppress interfacial reflections at hetero-structured interfaces, while the resistive FSS layer facilitates electromagnetic energy dissipation. Measurement results prove that the proposed three-layer structure exhibits a return loss below −10 dB from 4.06 to 20.68 GHz (corresponding to 134.4% fractional bandwidth). Additionally, to improve mechanical properties, the PU foam was modified with epoxy resin, increasing the elastic modulus to 12.6 MPa. The proposed composite structure offers significant potential for applications in multi-spectral compatible detection suppression.

Electronic Supplementary Material: Supplementary material (microstructure characterization, measurement setups, impedance matching characteristics, and electromagnetic properties) is available in the online version of this article at https://doi.org/10.26599/NR.2025.94907833.

Data availability

All data needed to support the conclusions in the paper are presented in the manuscript and the Electronic Supplementary Material. Additional data related to this paper may be requested from the corresponding author upon request.

Acknowledgements

This work was supported by the Postdoctoral Fellowship Program of CPSF (No. GZC20241620), the National Natural Science Foundation of China (Nos. 52222106, 52371171, 51971008, and 52121001), and the National Key Research and Development Program of China (No. 2021YBF3501304). We thank the researchers at the Analysis & Testing Center of Beihang University for their assistance with testing.

Declaration of competing interest

All the contributing authors report no conflict of interests in this work.

Author contribution statement

Z. R. R.: Conceptualization, writing – original draft. H. C. Y.: Methodology, investigation. C. L. Z.: Formal analysis. M. F.: Validation. L. Y.: Validation. X. S.: Data curation. J. Z. H.: Experimental design. X. F. L.: Supervision, writing – review & editing.

Use of AI statement

None.

References

[1] Li, B. D.; Deng, Y. L.; Liu, C.; Qiao, J.; Hou, S. Y.; Wu, N.; Wu, F.; Zeng, Z. H.; Liu, J. R. Rare earth oxides CeO_2 nanoparticle embedded magnetic carbon nanofibers for electro-magnetic cooperation and efficient electromagnetic wave absorption. *J. Mater. Sci. Technol.* **2025**, *217*, 1–8.

[2] Zheng, N.; Jia, B.; Liu, J.; Wang, X. J.; Zhang, D.; Zhang, H. R.; Wang, G. Q. Multi-strategy combined bionic coating for long-term robust protection against marine biofouling. *J. Mater. Sci. Technol.* **2025**, *210*, 265–277.

[3] Wu, N.; Yang, Y. F.; Wang, C. X.; Wu, Q. L.; Pan, F.; Zhang, R. N.; Liu, J. R.; Zeng, Z. H. Ultrathin cellulose nanofiber assisted ambient-pressure-dried, ultralight, mechanically robust, multifunctional MXene aerogels. *Adv. Mater.* **2023**, *35*, 2207969.

[4] Yan, J. T.; Cui, C.; Bai, W. H.; Tang, H.; Guo, R. H. Building of lightweight Nb_2CT_x MXene@Co nitrogen-doped carbon nanosheet arrays@carbon fiber aerogels for high-efficiency electromagnetic wave absorption in X and Ku bands inspired by sea cucumber. *Nano Res.* **2024**, *17*, 9261–9274.

[5] Zhang, Y. L.; Liu, A.; Tian, Y. Y.; Tian, Y. J.; Qi, X. S.; Qiu, H.; He, M. K.; Zhou, K.; Gu, J. W. Direct-ink-writing-printed aerogels with dynamically reversible thermal management and tunable electromagnetic interference shielding. *Adv. Mater.*, in press, DOI: 10.1002/adma.202505521.

[6] Qiao, J.; Song, Q. H.; Xuan, L. X.; Liu, J. R.; Zhang, X.; Zheng, S. N.; Lin, J. P.; Cai, W. Q.; Zhang, Q. D.; Zeng, Z. H. et al. Dual cross-linked magnetic MXene aerogel with high strength and durability enables multifunctionality. *Adv. Funct. Mater.* **2024**, *34*, 2401687.

[7] Zhang, H. Y.; Cao, F.; Xu, H.; Tian, W., Pan, Y.; Mahmood, N.; Jian, X. Plasma-enhanced interfacial engineering of FeSiAl@PUA@SiO_2 hybrid for efficient microwave absorption and anti-corrosion. *Nano Res.* **2023**, *16*, 645–653.

[8] Wu, Y.; Zhao, Y.; Zhou, M.; Tan, S. J.; Peymanfar, R.; Aslibeiki, B.; Ji, G. B. Ultrabroad microwave absorption ability and infrared stealth property of nano-micro CuS@rGO lightweight aerogels. *Nano-Micro Lett.* **2022**, *14*, 171.

[9] Ren, J.; Xie, C. W.; Zong, H.; Zhang, S. F.; Wu, S. L. Infrared stealth coating with tunable structural color based on ZnO spheres. *Small* **2024**, *20*, 2403549.

[10] Zhang, J. K.; Shi, J. M.; Zhao, D. P.; Wang, Q. C.; Wang, C. M. Realization of compatible stealth material for infrared, laser and radar based on one-dimensional doping-structure photonic crystals. *Infrared Phys. Technol.* **2017**, *85*, 62–65.

[11] He, M. K.; Hu, J. W.; Yan, H.; Zhong, X.; Zhang, Y. L.; Liu, P. B.; Kong, J.; Gu, J. W. Shape anisotropic chain-like CoNi/polydimethylsiloxane composite films with excellent low-frequency microwave absorption and high thermal conductivity. *Adv. Funct. Mater.* **2025**, *35*, 2316691.

[12] Fu, H. Q.; Fang, R. Q.; Tian, C.; Qian, W.; Cao, S. Y.; Zhang, Z. R.; Xu, X. X.; Yao, C.; Wang, Z.; He, D. P. High-performance thermal interface materials enabled by vertical alignment of lightweight and soft graphene foams. *Nano Res.* **2024**, *17*, 9293–9299.

[13] Li, C.; Liang, L. L.; Yang, Y.; Zhang, B. S.; Ji, G. B. Interfacial engineering of core–shell structured FeCoNi@SnO_2magnetic composites for tunable radar-infrared compatible stealth. *Chem. Eng. J.* **2024**, *481*, 148354.

[14] Deng, Y. M.; Ren, B.; Jia, Y. J.; Wang, Q.; Li, H. J. Layered composites made of polymer derived SiOC/ZrB_2 reinforced by ZrO_2/SiO_2 fibers with simultaneous microwave absorption and thermal insulation. *J. Mater. Sci. Technol.* **2024**, *196*, 50–59.

[15] Wu, G. B.; Dai, J. Y.; Shum, K. M.; Chan, K. F.; Cheng, Q.; Cui, T. J.; Chan, C. H. A universal metasurface antenna to manipulate all fundamental characteristics of electromagnetic waves. *Nat. Commun.* **2023**, *14*, 5155.

[16] Nam, J.; Chang, I.; Lim, J. S.; Woo, H.; Yook, J. G.; Cho, H. H. Flexible metasurface for microwave-infrared compatible camouflage via particle swarm optimization algorithm. *Small* **2023**, *19*, 2302848.

[17] Zhang, C.; Yang, J.; Yuan, W.; Zhao, J.; Dai, J. Y.; Guo, T. C.; Liang, J.; Xu, G. Y.; Cheng, Q.; Cui, T. J. An ultralight and thin metasurface for radar-infrared bi-stealth applications. *J. Phys. D: Appl. Phys.* **2017**, *50*, 444002.

[18] Sun, H. T.; Wang, J.; Zhu, R. C.; Chu, Z. T.; Fu, X. M.; Jia, Y. X.; Cui, Y. N.; Han, Y. J.; Qiu, T. S.; Sui, S. et al. Noninvasive inset-integrated meta-atom for achieving single-layer metasurface simultaneously with coded microwave reflectivity and digitalized infrared emissivity. *Nanophotonics* **2024**, *13*, 3113–3122.

[19] Meng, Z.; Tian, C. H.; Xu, C. L.; Wang, J. F.; Li, X. H.; Huang, S. N.; Fan, Q.; Qu, S. B. Optically transparent coding metasurface with simultaneously low infrared emissivity and microwave scattering reduction. *Opt. Express* **2020**, *28*, 27774–27784.

[20] Sun, C.; Zhao, K. Y.; Huang, M. L.; Luo, C. L.; Chen, X. D.; Wang, M. Structure regulating of metal clusters in carbonized metallic organic frameworks for high-efficient microwave absorption via tuning interaction strength between metals and ligands. *Nano Res.* **2024**, *17*, 1699–1709.

[21] Ren, Z. H.; Zhang, Z. X.; Wei, J. X.; Dong, B. W.; Lee, C. Wavelength-multiplexed hook nanoantennas for machine learning enabled mid-infrared spectroscopy. *Nat. Commun.* **2022**, *13*, 3859.

[22] Liu, X. H.; Wang, P.; Xiao, C. Y.; Fu, L. C.; Xu, J.; Zhang, D.; Zhou, H.; Fan, T. X. Compatible stealth metasurface for laser and infrared with radiative thermal engineering enabled by machine learning. *Adv. Funct. Mater.* **2023**, *33*, 2212068.

[23] Zhao, Z. H.; Qing, Y. C.; Kong, L.; Xu, H. L.; Fan, X. M.; Yun, J. J.; Zhang, L. M.; Wu, H. J. Advancements in microwave absorption motivated by interdisciplinary research. *Adv. Mater.* **2024**, *36*, 2304182.

[24] Wu, C.; Wang, J.; Zhang, X. H.; Kang, L. X.; Cao, X.; Zhang, Y. Y.; Niu, Y. T.; Yu, Y. Y.; Fu, H. L.; Shen, Z. J. et al. Hollow gradient-structured iron-anchored carbon nanospheres for enhanced electromagnetic wave absorption. *Nano-Micro Lett.* **2023**, *15*, 7.

[25] Cao, J. T.; Tao, J.; Yang, M. N.; Liu, C. J.; Yan, C. S.; Zhao, Y.; Yu, C. B.; Zhao, H. B.; Rao, W. H. A novel phosphorus-modified silica aerogel for simultaneously improvement of flame retardancy, mechanical and thermal insulation properties in rigid polyurethane foam. *Chem. Eng. J.* **2024**, *485*, 149909.

[26] Zhao, X.; Tang, X. W.; Qiao, Y. L.; Li, S. S.; Zhang, Z. H.; Lu, Y. Z.; Zhu, M. Y.; Hu, Z. Y.; Long, L. J.; Wang, Z. C. et al. Ultrathin

polyimide-based composites with efficient low-reflectivity electromagnetic shielding and infrared stealth performance. *Nano Res.* **2024**, *17*, 6700–6712.

[27] Zhang, Y. F.; Zhang, L.; Tang, L. F.; Du, R.; Zhang, B. L. S-NiSe/HG nanocomposites with balanced dielectric loss encapsulated in room-temperature self-healing polyurethane for microwave absorption and corrosion protection. *ACS Nano* **2024**, *18*, 8411–8422.

[28] Sun, C. Q.; Wang, Z. C.; Cao, W. X.; Gao, G.; Yang, L.; Han, J. C.; Zhu, J. Q. Preparation of brittle ITO microstructures using Laser-Induced forward transfer technology. *Chem. Eng. J.* **2024**, *496*, 153745.

[29] Shang, Y. Y.; Huang, C.; Li, Z.; Du, X. M. Bioinspired ultra-stretchable and highly sensitive structural color electronic skins. *Adv. Funct. Mater.* **2025**, *35*, 2412703.

[30] Zhang, Z. K.; Zhang, L. P.; Ren, Z. C.; Zhang, Y. K.; Hao, T. T.; Liu, D. Q.; Xu, L.; Liu, W. C.; Sun, J. W.; Ji, H. Y. et al. Multifunctional ultrathin metasurface with a low radar cross section and variable infrared emissivity. *ACS Appl. Mater. Interfaces* **2024**, *16*, 21109–21117.

[31] Qiu, J. F.; Peng, C. Y.; Wang, R. C.; Yao, C.; Liu, X.; Wang, Q.; Wang, W. One-step *in-situ* preparation of C/TiO_2@rGO aerogel derived from $Ti_3C_2T_x$ MXene for integrating microwave absorption, electromagnetic interference shielding and catalytic degradation of antibiotics. *Carbon* **2024**, *217*, 118610.

[32] Wu, L. H.; Liu, J.; Liu, X.; Mou, P. P.; Lv, H. M.; Liu, R.; Wen, J. G.; Zhao, J. C.; Li, J. L.; Wang, G. Z. Microwave-absorbing foams with adjustable absorption frequency and structural coloration. *Nano Lett.* **2024**, *24*, 3369–3377.

[33] Feng, M. F.; Zhang, K. F.; Cheng, H.; Li, Y.; Liu, B.; Liang, B. A nanocomposite metamaterial with excellent broadband microwave absorption performance and good mechanical property. *Compos. Sci. Technol.* **2023**, *239*, 110050.

[34] Zeng, X. J.; Nie, T. L.; Zhao, C.; Gao, Y. F.; Liu, X. F. *In situ* exsolution-prepared solid-solution-type sulfides with intracrystal polarization for efficient and selective absorption of low-frequency electromagnetic wave. *Adv. Sci.* **2024**, *11*, 2403723.

[35] Hou, Z. L.; Gao, X. S.; Zhang, J. Y.; Wang, G. S. A perspective on impedance matching and resonance absorption mechanism for electromagnetic wave absorbing. *Carbon* **2024**, *222*, 118935.

[36] Yu, Y. H.; Yi, P.; Xu, W. B.; Sun, X.; Deng, G.; Liu, X. F.; Shui, J. L.; Yu, R. H. Environmentally tough and stretchable MXene organohydrogel with exceptionally enhanced electromagnetic interference shielding performances. *Nano-Micro Lett.* **2022**, *14*, 77.

[37] Hou, Z. L.; Du, K. R.; Zhang, Y. Q.; Bi, S.; Zhang, J. Y. Nanoarchitectonics of MnO_2 nanotubes as sea urchin-like aggregates for dielectric response and microwave absorption with a wide concentration domain. *Nano Res.* **2023**, *16*, 2604–2610.

[38] Li, X. F.; Chen, C. Y.; Li, Z. Y.; Yi, P.; Zou, H. H.; Deng, G.; Fang, M.; He, J. Z.; Sun, X.; Yu, R. H. et al. Inter-skeleton conductive routes tuning multifunctional conductive foam for electromagnetic interference shielding, sensing and thermal management. *Nano-Micro Lett.* **2025**, *17*, 52.

[39] Chen, C. Y.; Li, X. F.; Yi, P.; Geng, Z.; Zou, H. H.; Deng, G.; Fang, M.; Yu, R. H.; Shui, J. L.; Liu, X. F. Chemically embedding CuS microspheres into MXene aerogel for strain-adaptive triple shielding of electromagnetic wave, heat and sound. *J. Mater. Sci. Technol.* **2025**, *224*, 80–91.

[40] Xiong, H.; Xie, J. Y.; Liu, Y. J.; Wang, B. X.; Xiao, D. P.; Zhang, H. Q. Microwave hyperthermia technology based on near-field focused metasurfaces: Design and implementation. *Adv. Funct. Mater.* **2025**, *35*, 2411842.

[41] An, Z. M.; Huang, Y. X.; Zhang, R. B. High-temperature multispectral stealth metastructure from the microwave-infrared compatible design. *Composites Part B: Eng.* **2023**, *259*, 110737.

[42] Gao, Z. Q.; Xu, C. L.; Tian, X. X.; Wang, J. F.; Tian, C. H.; Yang, B. Y.; Qu, S. B.; Fan, Q. Ultra-wideband flexible transparent metamaterial with wide-angle microwave absorption and low infrared emissivity. *Opt. Express* **2021**, *29*, 22108–22116.

[43] Han, M. Q.; Wei, X. Y.; Pei, L.; Zhu, F. J.; Jiang, Z. J.; Liu, S. J.; Chen, P. A hybrid metamaterial with broadband radar cross section reduction and low infrared emissivity for multispectral stealth. *J. Appl. Phys.* **2025**, *137*, 153106.

[44] Kang, J. F.; Kang, X. F.; Liu, S. Y.; Jing, H. H.; Wang, J. Y.; Qu, Z.; Duan, J. P.; Zhang, B. Z. Multifunctional-hierarchical flexibility metasurfaces for multispectral compatible camouflage of microwave, infrared and visible. *Opt. Express* **2023**, *31*, 29280–29299.

[45] Gao, Y. L.; Jing, H. H.; Wang, J. Y.; Kang, J. F.; Zhao, L.; Chen, L. Y.; Wang, Y. S.; Duan, J. P.; Qu, Z.; Zhang, B. Z. A transparent broadband flexible metamaterial absorber for radar infrared-compatible stealth. *J. Phys. D: Appl. Phys.* **2024**, *57*, 155102.

[46] Meng, Z.; Liu, D. Q.; Wang, J. F.; Pang, Y. Q.; Liu, T. W.; Jia, Y.; Gui, B. H.; Cheng, H. F. Metamaterial-inspired infrared electrochromic devices with wideband microwave absorption for multispectral camouflage. *Photonics Res.* **2024**, *12*, 2435–2446.

[47] Wang, Y. Z.; Luo, H. L.; Shao, Y. Z.; Wang, H.; Liu, T.; Wang, Z. J.; Liu, K. Y.; Su, X. G.; Xu, H. X. Detection and anti-detection with microwave-infrared compatible camouflage using asymmetric composite metasurface. *Adv. Sci.* **2024**, *11*, 2410364.

[48] Li, C.; Liang, L. L.; Zhang, B. S.; Yang, Y.; Ji, G. B. Magneto-dielectric synergy and multiscale hierarchical structure design enable flexible multipurpose microwave absorption and infrared stealth compatibility. *Nano-Micro Lett.* **2025**, *17*, 40.

[49] Wu, F. S.; Hu, P. Y.; Hu, F. Y.; Tian, Z. H.; Tang, J. W.; Zhang, P. G.; Pan, L.; Barsoum, M. W.; Cai, L. Z.; Sun, Z. M. Multifunctional MXene/C aerogels for enhanced microwave absorption and thermal insulation. *Nano-Micro Lett.* **2023**, *15*, 194.

[50] Shi, Y. N.; Ding, X. Y.; Pan, K. C.; Gao, Z. H.; Du, J.; Qiu, J. A novel multi-dimensional structure of graphene-decorated composite foam for excellent stealth performance in microwave and infrared frequency bands. *J. Mater. Chem. A* **2022**, *10*, 7705–7717.

[51] Li, Z. Y.; Xu, Y.; Wu, L. H.; Sun, Y. Zhang, M. N.; Dou, Z. F.; Zhao, J. C.; Yan, Y. Z.; Wang, G. Z. Carbon nanocage-in-microcage structure with tunable carbon-coated nickel as a microwave absorber with infrared stealth property. *Adv. Sci.* **2025**, *12*, 2412890.

[52] Yao, J. R.; Zhou, J. T.; Yang, F.; Peng, G. Y.; Liu, Y. J.; Yao, Z. J.; Wu, F.; Zeng, H. B. Multi-functional and multi-scenario applications for MXene aerogels with synergistically enhanced asymmetric modules. *Nano Res.* **2024**, *17*, 3359–3368.

[53] Yang, X.; Xuan, L. X.; Men, W. W.; Wu, X.; Lan, D.; Shi, Y. P.; Jia, H. X.; Duan, Y. P. Carbonyl iron/glass fiber cloth composites: Achieving multi-spectrum stealth in a wide temperature range. *Chem. Eng. J.* **2024**, *491*, 151862.

[54] Li, B. X.; Luo, Z.; Yang, W. G.; Sun, H.; Ding, Y.; Yu, Z. Z.; Yang, D. Z. Adaptive and adjustable MXene/reduced graphene oxide hybrid aerogel composites integrated with phase-change material and thermochromic coating for synchronous visible/infrared camouflages. *ACS Nano* **2023**, *17*, 6875–6885.

[55] He, M. K.; Zhong, X.; Lu, X. H.; Hu, J. W.; Ruan, K. P.; Guo, H.; Zhang, Y. L.; Guo, Y. Q.; Gu, J. W. Excellent low-frequency microwave absorption and high thermal conductivity in polydimethylsiloxane composites endowed by hydrangea-like CoNi@BN heterostructure fillers. *Adv. Mater.* **2024**, *36*, 2410186.

[56] Zhong, X.; He, M. K.; Zhang, C. Y.; Guo, Y. Q.; Hu, J. W.; Gu, J. W. Heterostructured BN@Co–C@C endowing polyester composites excellent thermal conductivity and microwave absorption at C band. *Adv. Funct. Mater.* **2024**, *34*, 2313544.

[57] Zhang, X.; Tian, X. L.; Wu, N.; Zhao, S. Y.; Qin, Y. T.; Pan, F.; Yue, S. Y.; Ma, X. Y.; Qiao, J.; Xu, W. et al. Metal-organic frameworks with fine-tuned interlayer spacing for microwave absorption. *Sci. Adv.* **2024**, *10*, eadl6498.

[58] Pan, F.; Shi, Y. Y.; Yang, Y.; Guo, H. T.; Li, L. X.; Jiang, H. J.; Wang, X.; Zeng, Z. H.; Lu, W. Porifera-inspired lightweight, thin, wrinkle-resistance, and multifunctional MXene foam. *Adv. Mater.* **2024**, *36*, 2311135.
[59] Zhang, Y. L.; Ruan, K. P.; Guo, Y. Q.; Gu, J. W. Recent advances of MXenes-based optical functional materials. *Adv. Photonics Res.* **2023**, *4*, 2300224.
[60] Tu, S. H.; Zhang, L. L.; Zhang, W. Z.; Feng, J. Waterborne recoatable transparent superhydrophobic coatings with excellent self-cleaning and anti-dust performance. *Small* **2025**, *21*, 2410171.
[61] Zhou, L.; Hu, P. F.; Bai, M.; Leng, N.; Cai, B.; Peng, H. L.; Zhao, P. Y.; Guo, Y. Q.; He, M. K.; Wang, G. S. et al. Harnessing the electronic spin states of single atoms for precise electromagnetic modulation. *Adv. Mater.* **2025**, *37*, 2418321.
[62] Zheng, S. N.; Xu, W. L.; Liu, J. R.; Pan, F.; Zhao, S. Y.; Wang, Y. D.; Zeng, Z. H.; Wu, N. One-hour ambient-pressure-dried, scalable, stretchable MXene/polyurea aerogel enables synergistic defense against high-frequency mechanical shock and electromagnetic waves. *Adv. Funct. Mater.* **2024**, *34*, 2402889.
[63] Wang, G.; Estevez, D.; Peng. M. Y.; Qin, F. X., Li, C. F.; Xu, P.; Wei, H. J. Boosting interfacial polarization through heterointerface engineering in MXene/graphene intercalated-based microspheres for electromagnetic wave absorption. *Nano-Micro Lett.* **2023**, *15*, 152.
[64] Han, Y. X.; Guo, H.; Qiu, H.; Hu, J. W.; He, M. K.; Shi, X. T.; Zhang, Y. L.; Kong, J.; Gu, J. W. Multimechanism decoupling for low-frequency microwave absorption hierarchical Fe-doped Co Magnetic microchains. *Adv. Funct. Mater.*, in press, DOI: 10.1002/adfm.202506803.
[65] Tang, L.; Jiang, J.; He, M. K.; Zhang, Y. L.; Hu, Q. Y.; Liu, X. L.; Liu, X.; Qiu, H. Lightweight PBO nanofiber@ZIF-67 derived carbon aerogel with superior electromagnetic wave absorption and thermal insulation. *J. Mater. Sci. Technol.* **2026**, *244*, 186–195.